Topological Hyperbolic Lattices

Sunkyu Yu,* Xianji Piao, and Namkyoo Park†
Photonic Systems Laboratory, Department of Electrical and Computer Engineering, Seoul National University, Seoul 08826, Korea

(Received 19 March 2020; accepted 7 July 2020; published 29 July 2020)

Non-Euclidean geometry, discovered by negating Euclid's parallel postulate, has been of considerable interest in mathematics and related fields for the description of geographical coordinates, Internet infrastructures, and the general theory of relativity. Notably, an infinite number of regular tessellations in hyperbolic geometry—hyperbolic lattices—are expected to extend Euclidean Bravais lattices and the consequent wave phenomena to non-Euclidean geometry. However, topological states of matter in hyperbolic lattices have yet to be reported. Here we investigate topological phenomena in hyperbolic geometry, exploring how the quantized curvature and edge dominance of the geometry affect topological phases. We report a recipe for the construction of a Euclidean photonic platform that inherits the topological band properties of a hyperbolic lattice under a uniform, pseudospin-dependent magnetic field, realizing a non-Euclidean analog of the quantum spin Hall effect. For hyperbolic lattices with different quantized curvatures, we examine the topological protection of helical edge states and generalize Hofstadter's butterfly, by employing two empirical parameters that measure the edge confinement and defect immunity. We demonstrate that the proposed platforms exhibit the unique spectral-magnetic sensitivity of topological immunity in highly curved hyperbolic planes. Our approach is applicable to general non-Euclidean geometry and enables the exploitation of infinite lattice degrees of freedom for band theory.

DOI: 10.1103/PhysRevLett.125.053901

Band theory in condensed-matter physics and photonics has been connected to the concept of topology [1–4]. The discovery of topologically nontrivial states has revealed a new phase of matter [3,4]. This phase offers the immunity of electronic conductance [1,3] or light transport [2,5–7] against disorder through topologically protected edge states.

A fundamental approach for generalizing band theory is to rethink the traditional assumptions regarding energy-momentum dispersion relations, such as static, Hermitian, and periodic conditions. In photonics, dynamical lattices enable one-way states in space-time Floquet bands [8]. Non-Hermitian photonics introduces novel band degeneracies [9] and topological phenomena [10]. Various studies have demonstrated perfect band gaps [11,12] and topological invariants [13–15] in disordered structures.

Most of the cornerstones in band theory have employed Euclidean geometry, because Bloch's theorem is well defined for a crystal, which corresponds to the uniform tessellation of Euclidean geometry. However, significant degrees of freedom are overlooked in Euclidean geometry because of a finite number of uniform Euclidean tessellations. For example, when considering a lattice with congruent unit cells, only six, four, or three nearest-neighbor interactions are allowed in two-dimensional (2D) Euclidean lattices [16–18]. Therefore, access to non-Euclidean geometry has been of considerable interest for employing more degrees of freedom in interelemental relationships of many-body systems. In circuit quantum electrodynamics, the extension of band structures to hyperbolic geometry was demonstrated [19], which revealed unique flat bands with spectral isolation. Although this cornerstone extends the concept of lattices from Euclidean to non-Euclidean geometry, the observed phenomena exploit only topologically "trivial" states.

Here, we demonstrate photonic topological phases of matter in hyperbolic geometry. Using the recursive gauge-field assignment, we design a "topological hyperbolic lattice": the lattice that is obtained from the regular tiling of the hyperbolic plane and is under a uniform effective magnetic field. We reveal frequency-selective and tunable topologically protected edge states with defect immunity as a non-Euclidean extension of the quantum spin Hall effect (QSHE). Our result is a step toward the non-Euclidean generalization of topological phenomena.

Among three homogeneous 2D geometries—elliptic, Euclidean, and hyperbolic planes—only Euclidean and hyperbolic planes belong to an infinite plane [16,17]. Thus, we focus on topological phenomena in 2D hyperbolic lattices. Hyperbolic lattices are obtained by generalizing Euclidean Bravais lattices to regular tiling: a tessellation of a plane using a single type of regular polygon. Each polygon vertex corresponds to a lattice element, while the polygon edge generalizes the Bravais vector. To visualize the hyperbolic plane, we employ the Poincaré disk [16,17]: the projection of a hyperboloid onto the unit disk [Figs. 1(a)–1(c), right].

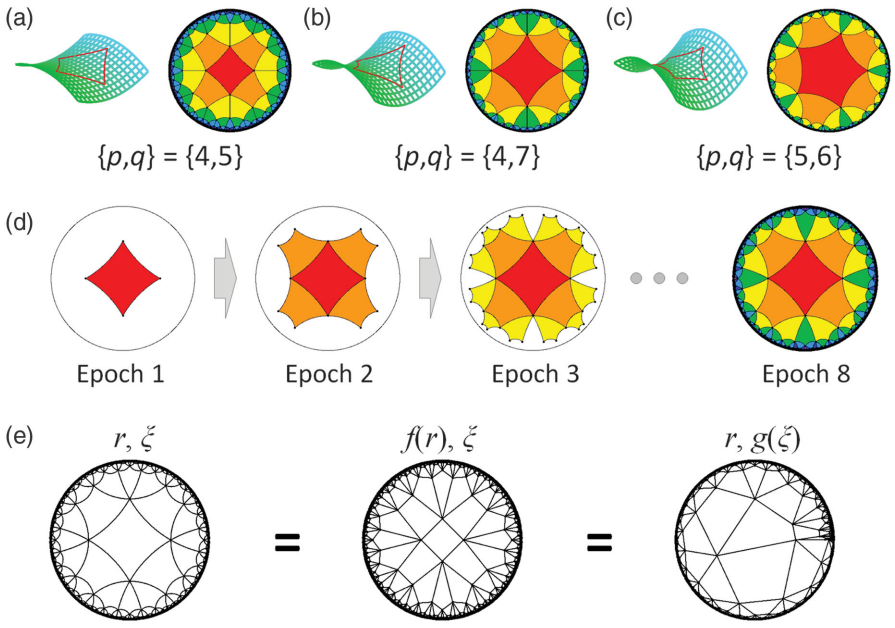

FIG. 1. Hyperbolic lattices. (a)–(c) (left) The saddle-shaped surface of the hyperbolic plane and (right) Poincaré disks for different K. (d) Recursive generation of the hyperbolic lattice $\{4, 6\}$. (e) A graph view of the hyperbolic lattice. For the original vertex positions in the polar coordinate (r, ξ), each deformed graph is obtained with $f(r) = r^2$ and $g(\xi) = \xi^2/(2\pi)$.

The negative curvature of the hyperbolic plane differentiates hyperbolic lattices from their Euclidean counterpart. A polygon in the hyperbolic plane has a smaller sum of internal angles than that of the Euclidean counterpart, permitting denser contact of the polygons at the vertices [Figs. 1(a)–1(c)]. For example, while only four squares can be contacted in a Euclidean square lattice, *any* number of squares greater than four can be contacted in hyperbolic lattices. Such "infinite" lattice degrees of freedom are expressed by the Schläfli symbol $\{p, q\}$, the contact of q p-sided regular polygons [16,17], as $\{4, q \geq 5\}$ for a square unit cell. With a seed polygon, each regular tiling is achieved by recursively adding neighboring polygons to the outermost edges per epoch [Fig. 1(d)], filling the unit disk at the infinite lattice limit. This recursive process implies treelike geometric properties of hyperbolic lattices.

Contrary to freely tunable areas of Euclidean polygons, the polygon area in the hyperbolic plane is restricted by the curvature of the plane and the sum of the internal angles [16,17]. The Gaussian curvature K of the hyperbolic lattice $\{p, q\}$ is determined as (Supplemental Material, Note S1 in [20])

$$K = -\frac{p\pi}{A_{\text{poly}}}\left(1 - \frac{2}{p} - \frac{2}{q}\right), \tag{1}$$

where A_{poly} is the area of the lattice unit polygon. For the same A_{poly}, the curvature K has a "quantized" value defined by $\{p, q\}$.

Because of the crinkling shapes of the hyperbolic plane, the realization of 2D hyperbolic lattices is extremely difficult, requiring complicated 3D structures [16,29]. To resolve this issue, we exploit the correspondence between graph networks and coupled-element systems [19,30], assigning graph vertices to elements and graph edges to interelemental interactions. When the identical interaction is assigned to all graph edges, the Hamiltonian of a coupled-element system depends only on the network structure of its graph representation. For the 2D Euclidean realization of a hyperbolic lattice, we employ the Poincaré disk as a graph. The identical interaction for all graph edges then leads to identical wave properties in the Poincaré disk and its deformed graphs [Fig. 1(e)].

To realize the Poincaré disk, we employ photonic coupled-resonator platforms, assigning each lattice site to the resonator that supports the pseudospins for clockwise ($\sigma = +1$) and counterclockwise ($\sigma = -1$) circulations [2]. The identical connection between lattice sites is realized by the coupling between resonators through a zero-field waveguide loop [Figs. 2(a)–2(c); Supplemental Material, Note S2 in [20]]. The coupling strength is independent of the real-space distance between the resonators and is determined by the evanescent coupling κ between the loop and the resonators: the same coupling strength in Figs. 2(a)–2(c). By introducing the phase difference between the upper ($+\varphi$) and lower ($-\varphi$) arms [Fig. 2(c)], the loop leads to the gauge field φ having a different sign for each pseudospin.

The suggested platform enables a real-space construction of the Poincaré disk [Fig. 2(d)], which inherits wave properties of a hyperbolic lattice. The structure is governed by the photonic tight-binding Hamiltonian (Supplemental Material, Note S2 in [20])

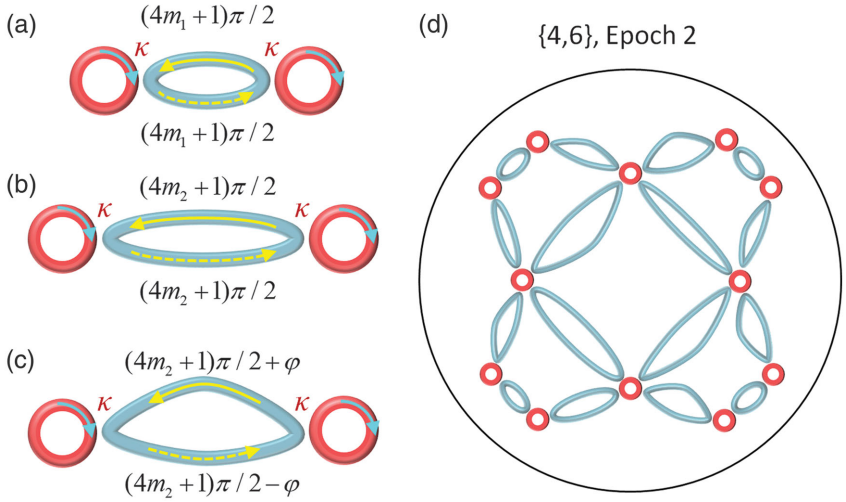

FIG. 2. Photonic hyperbolic lattices. (a)–(c) Coupling schematics for the identical connection between lattice sites. (d) An example of photonic hyperbolic lattices: $\{4, 6\}$ lattice at the epoch 2.

$$H = \sum_{m,\sigma} \omega_m a^\dagger_{m\sigma} a_{m\sigma} + t \sum_{\langle m,n\rangle,\sigma} (e^{-i\sigma\varphi_{mn}} a^\dagger_{m\sigma} a_{n\sigma} + \text{H.c.}), \quad (2)$$

where ω_m is the resonance frequency of the mth resonator site, $a^\dagger_{m\sigma}$ (or $a_{m\sigma}$) is the creation (or annihilation) operator for the σ pseudospin at the mth site, $t = \kappa^2/2$ is the coupling strength between the sites, φ_{mn} is the additionally acquired phase from the nth to mth sites, the pair $\langle m, n\rangle$ is determined by the graph edge of the Poincaré disk, and H.c. denotes the Hermitian conjugate. At this stage, we set the identical resonance frequency as $\omega_m = \omega_0$, where ω_0 is constant. The practical implementation of the Poincaré disk is restricted by the geometric nature of hyperbolic lattices: the scale-invariant distance between resonators (Supplemental Material, Note S3 in [20]).

In analyzing the Poincaré-disk wave structure, we consider "finite" and "spin-degenerate" structures. First, due to the lack of commutative translation groups and Bravais vectors in hyperbolic geometry, Bloch's theorem cannot be applied to hyperbolic lattices [19]. We instead apply numerical diagonalization to the Hamiltonian H in Eq. (2) for finite but large hyperbolic lattices (six-epoch generation for each lattice configuration throughout this Letter). The difference in analyzing hyperbolic lattices compared to the conventional eigenstate calculation of finite Euclidean lattices [2,8] is in the nearest-neighbor pair $\langle m, n\rangle$ determined by the Poincaré disk. Second, because pseudospin modes experience the same magnetic field strength with the opposite sign, the consequent band structures of both pseudospins are identical when spin mixing is absent [2]. Assuming this spin degeneracy, we focus on the $\sigma = +1$ pseudospin. From these conditions, we observe extended flat bands in hyperbolic lattices for topologically trivial cases (Supplemental Material, Note S4 in [20]).

We now investigate the photonic QSHE [2,4] in hyperbolic square lattices, which we call the hyperbolic QSHE. The uniqueness of the hyperbolic QSHE stems from noncommutative translation groups in hyperbolic geometry [17,19], which prohibit the natural counterpart of Bravais lattices. When constructing a uniform magnetic field in topological Euclidean lattices, a "Landau gauge"—the linearly increasing gauge field along one of the Bravais vectors—is usually employed [1–4,8,31,32]. However, this Landau gauge cannot be implemented in hyperbolic geometry due to the absence of Bravais vectors. We instead propose the tree-type design of a "hyperbolic gauge" for the hyperbolic QSHE [Figs. 3(a) and 3(b)]. In this design, the unit cell area A_{poly} is effectively the same for the entire class of $\{4, q \geq 5\}$ (setting $A_{\text{poly}} = 1$), because the indirect coupling strength t is set to be the same.

Consider the target magnetic flux θ through each unit polygon of a hyperbolic lattice. We assign gauge fields equally to each edge of the seed polygon [blue solid arrows in Fig. 3(a)]. For the polygons in the next epoch [Fig. 3(b)], after evaluating the predefined gauge fields (blue dashed arrows), we calculate the deficient gauge for the target flux θ and then assign the necessary average gauge to each undefined polygon edge (green solid arrows). The recursive process leads to the gauge configuration that achieves a uniform magnetic field ($B = \theta$) through the entire polygons [Fig. 3(c)] as the hyperbolic counterpart of the Landau gauge. The suggested procedure is applicable to *any* geometry under an arbitrary magnetic field, including elliptic geometry and nonuniform magnetic fields.

When analyzing topological phenomena in hyperbolic lattices, we cannot apply the well-known reciprocal-space formulation of the Chern number due to the absence of Bravais vectors. We instead employ an empirical quantity $C^{(n)}_{\text{edge}}$ [33]

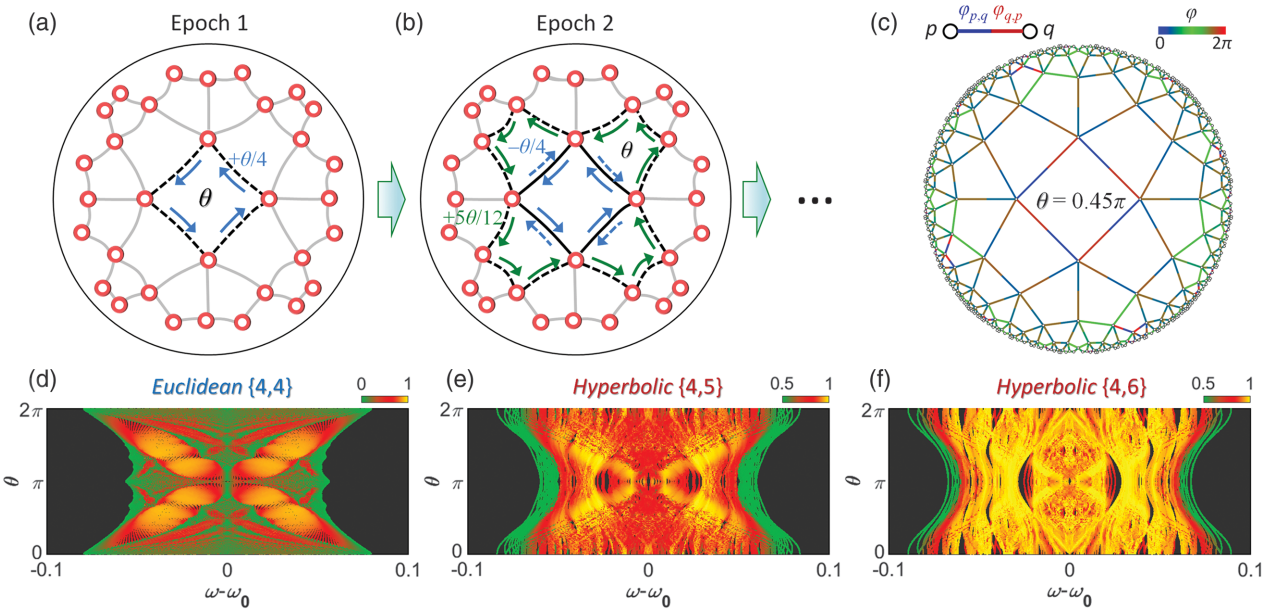

FIG. 3. Hyperbolic QSHE. (a)–(c) Hyperbolic gauge for a uniform magnetic field: (a) seed polygon, (b) polygons in the next epoch, and (c) the final result. The blue and green arrows in (a) and (b) denote the gauge field assigned in the first and second epoch, respectively. $\varphi_{q,p}$ in (c) represents the gauge field from the pth to qth element. (d)–(f) $C_{\text{edge}}^{(n)}$ as a function of ω and θ: (d) Euclidean lattice with $K = 0$, and (e),(f) hyperbolic lattices of (e) $K = -1.26$ and (f) $K = -2.09$. $\omega_0 = 1$. All other parameters are the same as those in Fig. 2.

$$C_{\text{edge}}^{(n)} = \frac{\sum_{r\in\Lambda_{\text{edge}}} |\psi_r^{(n)}|^2}{\sum_{r=1}^{N} |\psi_r^{(n)}|^2}, \tag{3}$$

where r denotes each lattice element, N is the total number of elements, $\psi_r^{(n)}$ is the field amplitude of the nth eigenstate at the rth element, and Λ_{edge} is the set of the boundary elements of the system. $C_{\text{edge}}^{(n)}$ measures the spatial energy concentration at the system boundary and has been applied to quantify the topological phase in aperiodic systems [33].

Figures 3(d)–3(f) show $C_{\text{edge}}^{(n)}$ in Euclidean [Fig. 3(d)] and hyperbolic lattices [Figs. 3(e) and 3(f)] at each eigenfrequency ω for the magnetic field $B = \theta$. Figure 3(d) presents the spectrum analogous to Hofstadter's butterfly [31], where the regions of high $C_{\text{edge}}^{(n)}$ depict topologically protected helical edge states [1–4,34]. In contrast, hyperbolic lattices generally lead to a much higher $C_{\text{edge}}^{(n)}$ than the Euclidean lattice [Figs. 3(e) and 3(f) with the color range $0.5 \leq C_{\text{edge}}^{(n)} \leq 1.0$], showing stronger energy confinement on the system boundary. This boundary-dominant behavior is explained by the treelike geometric nature of hyperbolic lattices: more boundary elements in a more curved geometry, analogous to more leaves on a tree with more branches (Supplemental Material, Note S5 in [20]). This geometrical origin also clarifies that a high $C_{\text{edge}}^{(n)}$ does not guarantee "topological protection," as shown in Eq. (3): quantifying the energy concentration at the system boundary, not measuring the topological quantity or its related property, such as disorder-immune behaviors. For example, a high density of topologically trivial edge states prohibits the finding of topologically protected states through $C_{\text{edge}}^{(n)}$.

To extract topologically protected states from a high density of edge states, we examine the scattering from hyperbolic QSHE systems. We employ input and output waveguides that are evanescently coupled to the selected elements at the system boundary [Figs. 4(a) and 4(b)] and then evaluate the transmission against disorder. We focus on spin-mixing-free diagonal disorder [2], which may originate from imperfections in the radii or refractive indices of optical resonators. Diagonal disorder is introduced by assigning random perturbations to the resonance frequency of each element, as $\omega_m = \omega_0 + \text{unif}[-\Delta, +\Delta]$, where $\text{unif}[a, b]$ is a uniform random distribution between a and b and Δ is the maximum perturbation strength.

Figure 4(c) shows the transmission spectrum with a nonzero magnetic field for different realizations of disorder. We observe spectral bands with high transmission (points **a** and **b**), which correspond to topologically protected helical edge states with backward or forward rotations [Figs. 4(a) and 4(b)]. As shown in the small deviation of the transmission, the topologically protected states achieve defect immunity.

To identify this topological protection, we introduce a new empirical parameter that measures the disorder-immune transmission: $C_{\text{immune}}(\omega, \theta) = E[t(\omega, \theta)]$, where $E[\ldots]$ denotes the expectation value and $t(\omega, \theta)$ is the power

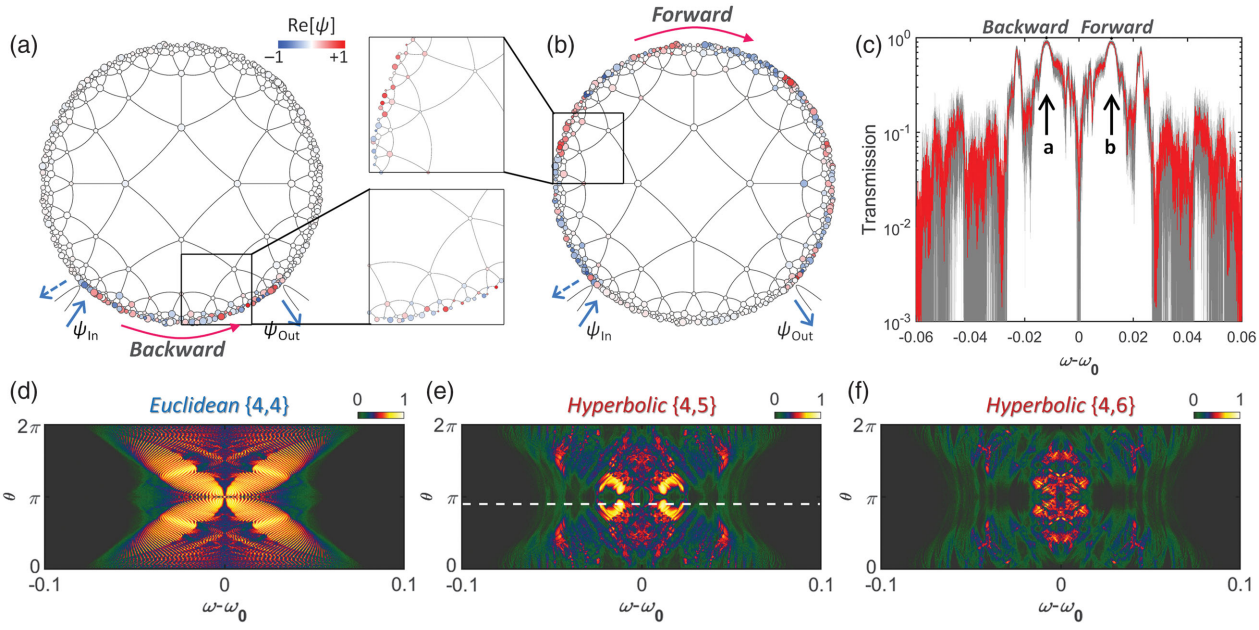

FIG. 4. Topological protection and Hofstadter's "hyperbolic" butterflies. (a),(b) Transmission through topologically protected edge states in the lattice $\{4,5\}$: (a) backward ($t = 99.50\%$) and (b) forward ($t = 98.51\%$) transmission [black arrows in (c)]. Different radii of the elements represent diagonal disorder. (c) Transmission spectrum at $B = \theta = 0.9\pi$ (red line, average; gray regions, standard deviation). (d)–(f) C_{immune} for (d) Euclidean and (e),(f) hyperbolic lattices. For the cases in (c)–(f), we examine an ensemble of 50 realizations of disorder. The case in (c) denotes the white dashed line in (e). $\Delta = \omega_0/200$ for all cases. The coupling between the boundary elements and the input or output waveguide is $0.08\omega_0$. All other parameters are the same as those in Fig. 3.

transmission spectrum for each realization of disorder at a magnetic field $B = \theta$. We compare $C_{\text{immune}}(\omega, \theta)$ in Euclidean [Fig. 4(d)] and hyperbolic lattices with different curvatures K [Figs. 4(e) and 4(f)], achieving the hyperbolic counterpart of the Hofstadter butterfly: the narrower spectral-magnetic (ω-θ) bandwidth of topological protection for larger $|K|$. Furthermore, while the Euclidean lattice presents a C_{immune} map analogous to the conventional Hofstadter butterfly [31,35] [Fig. 4(d)], the C_{immune} maps for hyperbolic lattices [Figs. 4(e) and 4(f)] display a significant discrepancy from the $C^{(n)}_{\text{edge}}$ maps in Figs. 3(e) and 3(f). This distinction demonstrates that C_{immune} extracts "disorder-immune" topologically protected edge states from the entire (topologically trivial or nontrivial) edge states.

Despite the continuous Schläfli symbols of Euclidean $\{4,4\}$ and hyperbolic $\{4, q \geq 5\}$ lattices, the patterns of Hofstadter's butterflies are classified according to the lattice geometry. This distinction emphasizes different *intrinsic* geometries of Euclidean and hyperbolic planes [16,17], which lead to the quantized polygon angle sum depending on $\{p, q\}$ (Supplemental Material, Note S1 in [20]). Such a distinct unit polygon results in $\{p, q\}$-quantized interelemental interactions, which differentiate the pattern of the Hofstadter's butterfly in each lattice.

Because of the lack of periodicity in hyperbolic lattices, the interpretation of a fractal energy spectrum in Hofstadter's butterfly, focusing on the commensurability between the period and magnetic length [31,35], cannot be straightforwardly extended to hyperbolic counterparts. Instead, the origin of the narrower ω-θ bandwidths of the topological protection in hyperbolic lattices [Figs. 4(e) and 4(f)] is explained by their boundary-dominant geometry (Supplemental Material, Note S5 in [20]). A high density of topologically trivial edge states from the boundary-dominant geometry hinders the exclusive excitation of topologically nontrivial edge states. The general trend of the narrower ω-θ bandwidth due to more enhanced boundary dominance is maintained for higher q values (Supplemental Material, Note S6 in [20]).

The result in Fig. 4 shows that increased lattice degrees of freedom in non-Euclidean geometry allow control of topologically protected functionalities by exploiting new patterns of Hofstadter's butterflies. For example, topological hyperbolic lattices with the narrower ω-θ bandwidth enable frequency-selective and tunable wave propagations while preserving defect immunity (Supplemental Material, Note S7 in [20] for switching of topologically protected propagations with high on-off ratios). This result also implies that non-Euclidean geometry with smaller q values—elliptic geometry—will also provide extended design freedom by manipulating ω-θ responses.

We have demonstrated topological properties in hyperbolic geometry. By employing a tree-type gauge design, we achieved a topological hyperbolic lattice that leads to the hyperbolic counterpart of the QSHE. Using two empirical parameters that measure the edge confinement ($C^{(n)}_{\text{edge}}$) and

defect immunity (C_{immune}), we classified a high density of edge states in hyperbolic lattices in terms of topological protection. With the narrower ω-θ bandwidth for defect immunity in hyperbolic lattices, we expect frequency-selective and modulation-sensitive photonic devices with error robustness. Our approach also inspires topological hyperbolic lattices in acoustics [34] or cold atoms [32].

As observed in distinct patterns of Hofstadter's Euclidean and hyperbolic butterflies, hyperbolic lattices are topologically distinguished from Euclidean lattices in terms of band theory. This topological uniqueness is emphasized with the geometrical nature of hyperbolic lattices: the scale invariance and high edge-to-bulk ratio. We expect the use of the geometrical nature of hyperbolic geometry, which will impose scale-free properties on materials [36], as implied in Internet infrastructures [24]. A real-space construction of hyperbolic lattices using origami design [29] or nanophotonic curved space [37–40] may also be of interest.

We acknowledge financial support from the National Research Foundation of Korea (NRF) through the Global Frontier Program (2014M3A6B3063708), the Basic Science Research Program (2016R1A6A3A04009723), and the Korea Research Fellowship Program (2016H1D3A1938069), all funded by the Korean government.

*sunkyu.yu@snu.ac.kr
†nkpark@snu.ac.kr

[1] C. L. Kane and E. J. Mele, Quantum Spin Hall Effect in Graphene, Phys. Rev. Lett. **95**, 226801 (2005).
[2] M. Hafezi, E. A. Demler, M. D. Lukin, and J. M. Taylor, Robust optical delay lines with topological protection, Nat. Phys. **7**, 907 (2011).
[3] M. Z. Hasan and C. L. Kane, Colloquium: Topological insulators, Rev. Mod. Phys. **82**, 3045 (2010).
[4] T. Ozawa, H. M. Price, A. Amo, N. Goldman, M. Hafezi, L. Lu, M. C. Rechtsman, D. Schuster, J. Simon, O. Zilberberg, and I. Carusotto, Topological photonics, Rev. Mod. Phys. **91**, 015006 (2018).
[5] F. Haldane and S. Raghu, Possible Realization of Directional Optical Waveguides in Photonic Crystals with Broken Time-Reversal Symmetry, Phys. Rev. Lett. **100**, 013904 (2008).
[6] Z. Wang, Y. Chong, J. D. Joannopoulos, and M. Soljačić, Observation of unidirectional backscattering-immune topological electromagnetic states, Nature (London) **461**, 772 (2009).
[7] M. C. Rechtsman, J. M. Zeuner, Y. Plotnik, Y. Lumer, D. Podolsky, F. Dreisow, S. Nolte, M. Segev, and A. Szameit, Photonic Floquet topological insulators, Nature (London) **496**, 196 (2013).
[8] K. Fang, Z. Yu, and S. Fan, Realizing effective magnetic field for photons by controlling the phase of dynamic modulation, Nat. Photonics **6**, 782 (2012).
[9] M.-A. Miri and A. Alù, Exceptional points in optics and photonics, Science **363**, eaar7709 (2019).
[10] H. Shen, B. Zhen, and L. Fu, Topological Band Theory for Non-Hermitian Hamiltonians, Phys. Rev. Lett. **120**, 146402 (2018).
[11] W. Man, M. Florescu, E. P. Williamson, Y. He, S. R. Hashemizad, B. Y. Leung, D. R. Liner, S. Torquato, P. M. Chaikin, and P. J. Steinhardt, Isotropic band gaps and freeform waveguides observed in hyperuniform disordered photonic solids, Proc. Natl. Acad. Sci. U.S.A. **110**, 15886 (2013).
[12] S. Yu, X. Piao, J. Hong, and N. Park, Bloch-like waves in random-walk potentials based on supersymmetry, Nat. Commun. **6**, 8269 (2015).
[13] A. Kitaev, Anyons in an exactly solved model and beyond, Ann. Phys. (Amsterdam) **321**, 2 (2006).
[14] R. Bianco and R. Resta, Mapping topological order in coordinate space, Phys. Rev. B **84**, 241106 (2011).
[15] N. P. Mitchell, L. M. Nash, D. Hexner, A. M. Turner, and W. T. Irvine, Amorphous topological insulators constructed from random point sets, Nat. Phys. **14**, 380 (2018).
[16] J. R. Weeks, *The Shape of Space* (CRC press, Boca Raton, FL, 2001).
[17] M. J. Greenberg, *Euclidean and Non-Euclidean Geometries: Development and History*, 4th ed. (Macmillan, London, 2008).
[18] J. D. Joannopoulos, S. G. Johnson, J. N. Winn, and R. D. Meade, *Photonic Crystals: Molding the Flow of Light* (Princeton University Press, Princeton, NJ, 2011).
[19] A. J. Kollár, M. Fitzpatrick, and A. A. Houck, Hyperbolic lattices in circuit quantum electrodynamics, Nature (London) **571**, 45 (2019).
[20] See Supplemental Material at http://link.aps.org/supplemental/10.1103/PhysRevLett.125.053901 for (Note S1) quantized curvatures of hyperbolic lattices, (Note S2) derivation of the photonic tight-binding Hamiltonian, (Note S3) distance between resonators and its effect on practical implementation, (Note S4) extended flat bands in topologically trivial hyperbolic lattices, (Note S5) edge dominance in hyperbolic lattices, (Note S6) extended data for higher q values, and (Note S7) efficient modulation in Hofstadter's hyperbolic butterflies, which includes Refs. [21–28].
[21] H. A. Haus, *Waves and Fields in Optoelectronics* (Prentice-Hall, Englewood Cliffs, NJ, 1984), Vol. 464.
[22] A.-L. Barabási and R. Albert, Emergence of scaling in random networks, Science **286**, 509 (1999).
[23] A.-L. Barabási and E. Bonabeau, Scale-free networks, Sci. Am. **288**, 60 (2003).
[24] M. Boguná, F. Papadopoulos, and D. Krioukov, Sustaining the internet with hyperbolic mapping, Nat. Commun. **1**, 62 (2010).
[25] S. Mittal, V. V. Orre, G. Zhu, M. A. Gorlach, A. Poddubny, and M. Hafezi, Photonic quadrupole topological phases, Nat. Photonics **13**, 692 (2019).
[26] H. Lee, T. Chen, J. Li, K. Y. Yang, S. Jeon, O. Painter, and K. J. Vahala, Chemically etched ultrahigh-Q wedge-resonator on a silicon chip, Nat. Photonics **6**, 369 (2012).
[27] S.-Y. Xu, Y. Xia, L. Wray, S. Jia, F. Meier, J. Dil, J. Osterwalder, B. Slomski, A. Bansil, and H. Lin, Topological phase transition and texture inversion in a tunable topological insulator, Science **332**, 560 (2011).
[28] M. Finazzi, M. Savoini, A. Khorsand, A. Tsukamoto, A. Itoh, L. Duo, A. Kirilyuk, T. Rasing, and M. Ezawa, Laser-Induced

Magnetic Nanostructures with Tunable Topological Properties, Phys. Rev. Lett. **110**, 177205 (2013).
[29] S. J. Callens and A. A. Zadpoor, From flat sheets to curved geometries: Origami and kirigami approaches, Mater. Today **21**, 241 (2018).
[30] S. Yu, X. Piao, J. Hong, and N. Park, Interdimensional optical isospectrality inspired by graph networks, Optica **3**, 836 (2016).
[31] D. R. Hofstadter, Energy levels and wave functions of Bloch electrons in rational and irrational magnetic fields, Phys. Rev. B **14**, 2239 (1976).
[32] D. Jaksch and P. Zoller, Creation of effective magnetic fields in optical lattices: The Hofstadter butterfly for cold neutral atoms, New J. Phys. **5**, 56 (2003).
[33] C. Liu, W. Gao, B. Yang, and S. Zhang, Disorder-Induced Topological State Transition in Photonic Metamaterials, Phys. Rev. Lett. **119**, 183901 (2017).
[34] Z. Yang, F. Gao, X. Shi, X. Lin, Z. Gao, Y. Chong, and B. Zhang, Topological Acoustics, Phys. Rev. Lett. **114**, 114301 (2015).
[35] G. Wannier, A result not dependent on rationality for Bloch electrons in a magnetic field, Phys. Status Solidi B **88**, 757 (1978).
[36] S. Yu, X. Piao, and N. Park, Machine learning identifies scale-free properties in disordered materials, arXiv: 2003.07011v2.
[37] R. Bekenstein, J. Nemirovsky, I. Kaminer, and M. Segev, Shape-Preserving Accelerating Electromagnetic Wave Packets in Curved Space, Phys. Rev. X **4**, 011038 (2014).
[38] C. Sheng, R. Bekenstein, H. Liu, S. Zhu, and M. Segev, Wavefront shaping through emulated curved space in waveguide settings, Nat. Commun. **7**, 1 (2016).
[39] E. Lustig, M.-I. Cohen, R. Bekenstein, G. Harari, M. A. Bandres, and M. Segev, Curved-space topological phases in photonic lattices, Phys. Rev. A **96**, 041804 (2017).
[40] R. Bekenstein, Y. Kabessa, Y. Sharabi, O. Tal, N. Engheta, G. Eisenstein, A. J. Agranat, and M. Segev, Control of light by curved space in nanophotonic structures, Nat. Photonics **11**, 664 (2017).